INTEGRATED SENSING AND COMMUNICATIONS VIA 5G NR WAVEFORM: PERFORMANCE ANALYSIS

Yuanhao Cui, Xiaojun Jing, Junsheng Mu

Beijing University of Posts and Telecommunications

ABSTRACT

Nowadays, a possible approach to designing a commercial-attractive sensing solution is integrating sensing capability into widely deployed communication systems, e.g., the force coming fifth-generation (5G) new radio (NR), by slightly modifying the standard. To this end, in this paper, we firstly investigate the possibility of re-using the NR waveform for sensing by reviewing current NR frame structure. Then, the self-ambiguity and cross-ambiguity functions are analyzed to exploit the NR waveform performance limitations. Several synchronizations and reference NR signal structures are considered for both downlink and uplink NR transmissions. Finally, the simulated NR frame and its self- and cross-ambiguity simulation results demonstrate the performance limitations.

Index Terms— Integrated Sensing and Communications, Joint Radar and Communications, Ambiguity Function

1. INTRODUCTION

A communication- and sensing-capable radio emission would simultaneously extract the situational environmental information and convey communication data from the transmitter to the intended receiver(s), this type of research is typically referred to as Integrated Sensing And Communication (ISAC) [1, 2, 3]. Even though a number of potential signaling strategy candidates can achieve various ISAC levels [4, 5], the most straightforward implementable approach is to reuse communication infrastructures for wireless sensing, with a low-cost and fast-deployment footprint [1]. Motivated by a force coming fifth-generation (5G) new radio (NR), in this paper, we investigate the sensing performance of current NR waveform by ambiguity analysis, particularly focusing on various standardized signal structures, to answer whether the standardized signal structure can be used for sensing.

In general, there were various researchers tried to investigate sensing performance, e.g., detection performance by the generalized likelihood ratio test (GLRT) [6], estimation performance by the Cramér–Rao lower bound (CRLB) [7], stochastic geometry by the outage probability, and beampattern analysis for the spatial beamforming design [8, 9]. However, as one of the main sensing performance analysis tools, although the ambiguity function of LTE waveform [10, 11] has been analyzed in passive radar literature, to the best of our knowledge, the ambiguity performance of the NR waveform has not been well studied yet.

In this paper, we exploit the possibility of enabling sensing functions by providing a short overview on the related NR standard contents. Considering several standardized signal structures can be treated as a prior to conduct a partially matched filter, we then evaluate the self- and cross-ambiguity functions for various NR signal structures, including the synchronization signals (SS) block, the reference signals such as CSI-RS. In order to evaluate the sensing performance, we employ the calculated self- and cross- ambiguity function in a systematic NR waveform scenario to indicate which signal structure in current NR waveform would be better for sensing usage. The simulations include the self-ambiguity performance of a SS block, and the cross-ambiguity performance between a SS block and a SS burst/a half NR frame. Our result confirms that current NR waveform can be re-used for sensing functionality, however, the low matched filter gain appears to be a new challenge.

2. 3GPP NR OVERVIEW AND TRANSMISSION CHARACTERISTICS

Different with the LTE, in the 3GPP NR release 15 [12], flexible signaling strategies brings both challenges and opportunities for the sensing usage. Numerology $\mu = \{0, 1, ..., 4\}$ govern the parameters of generated Orthogonal Frequency Division Multiplexing (OFDM) waveform, which are key to support such a wide range of frequencies and deployments. A cyclic prefix (CP) is employed at the beginning of each OFDM symbol to mitigate the multipath effects. However, different from the CP deployment in LTE, a variable CP duration, also known as scalable subcarrier spacing (SCS), is suggested as a superset of 15kHz, as $\Delta f^{\mu} = 2^{\mu} \times 15$ Hz and controlled by μ. According to current standards [13], $\mu = \{0, 1, 2\}$ are used in frequency range 1 (FR1), resulting in 15/30/60 kHz SCS values and up to 100 MHz single carrier bandwidth. In order to remedy worsening phase noise and Doppler shift in high frequencies, frequency range 2 (FR2) adopts $\mu = \{3, 4\}$ with 120/240 kHz SCS and up to 400 MHz single carrier bandwidth. Same with LTE standards, the time

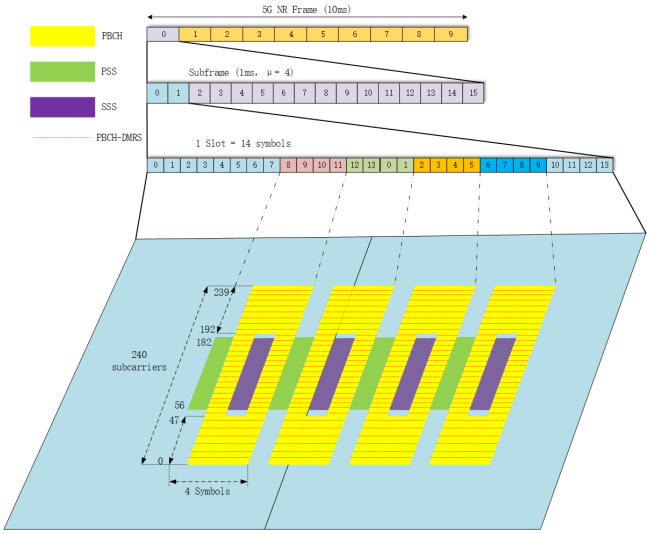

Fig. 1: The structure of a NR SSB are illustrated [14].

duration of an NR frame and a subframe are 10ms and 1ms as illustrated in Fig.1, respectively. Consequently, we could observe that range resolution of NR waveform varies with μ, both in the sub-6G bands (i.e. FR1) and the millimeter wave bands (i.e. FR2).

2.1. Synchronization and Reference Signals

Roughly, a pseudo-random coded OFDM waveform would achieve better self-correlation performance than uncoded OFDM waveform, which also results in the better matched filter gain. From this viewpoint, both synchronization and reference signals are better candidates. In the NR downlink, the Primary Synchronization Signals (PSS), Secondary Synchronization Signals (SSS), Physical Broadcast Channel (PBCH), and its Demodulation Reference Signals (DMRS) are collected to construct a SS block, which is a "always-on" signal structure as illustrated in Fig.1. In general, PSS are generated by mapping a 127-length M-sequence mapping to 127 BPSK modulated OFDM subcarriers and transmitted in the first OFDM symbol. Similarly, the SSS are generated as a BPSK modulated Gold-sequence of length 127 with the third OFDM symbol. A 31-length Gold-sequence is used to demodulate PBCH, termed as PBCH-DMRS. Although PBCH is not generated from the pseudo-random sequence, its 24-bit data payload only carries cell identity information.

On the other hand, differ with LTE, the deployment of SS blocks is flexible and adjustable both in the time and frequency domain. In frequency domain, the initial subcarrier position of SS block can be obtained from the hyper-layer parameter *OffsetToPointA* and *ssb-SubcarrierOffset*. In the time domain, up to 64 SS blocks are grouped into a *SS burst set* within a 5ms time window limitation. The transmission pattern of a SS burst set depends on hyper-layer parameter *ssb-PositionsInBurst* and numerology, as illustrated in Fig.2. Based on the above brief overview, we provide several observations:

- If a NR base station is sensing surrounding environment (i.e., a downlink mono-static sensing scenarios), the received sensing echoes can be analyzed straightforwardly, because the transmitted NR waveform is known at base station (BS) side.
- If the transmitter and receiver are separated (i.e., a downlink bi-static sensing configuration like a BS to a user requirement (UE)), the SS blocks can be employed for sensing at the UE side. The main reason is, the above mentioned signal structure is predetermined in a certain NR cell, such that they can be treated as *a prior* to conduct a partially matched filter at user equipments. [2].
- Although the range and Doppler resolutions are depending on the NR parameters, particularly μ. However, differ with LTE, NR physical layer provides a room to employ novel time and frequency transmission patterns to achieve super range and Doppler resolution.

2.2. 3GPP 38.211 OFDM Signal Model

Time-continuous OFDM baseband signal in [12, 5.3.1] is uniformly defined by 4-D tuple $(k,l)_{p,\mu}$, where p is antenna port, μ is subcarrier spacing configuration parameter, $k \in \{0,1,...,N^{\mu}-1\}$ denotes subcarrier index in frequency domain and $l \in \{0,1,...,L-1\}$ denotes symbol position in time domain. The L-length baseband OFDM block can be simplified as,

$$s^{(p,\mu)}(t) = \sum_{l=0}^{L-1}\sum_{k=0}^{N^{\mu}-1} a_{k,l}^{(p,\mu)} e^{j2\pi k\Delta f^{\mu} t} \text{rect}\left(\frac{t - N_{sym,l}^{\mu} T_c}{N_{sym,l}^{\mu} T_c}\right). \tag{1}$$

Here $a_{k,l}^{(p,\mu)}$ is the value of resource elements with total signal energy $\sum_{l=0}^{L-1}\sum_{k=0}^{N^{\mu}-1}|a_{k,l}|^2 = E_p$; subcarrier spacing Δf^{μ} is controlled by numerology parameter μ and related higher-layer parameters. Considering flexible subcarrier spacing, the OFDM basic time unit T_c is introduced in 3GPP 38.211 with responding to the minimum $\Delta f_{\min}^{\mu}$, shown as $T_c = 1/(\Delta f_{\max}^{\mu} \cdot N_{FFT}) = 1/(480\times10^3\times4096) = 0.509ns$, where N_{FFT} is the size of Fast Fourier Transform (FFT) matrix. Therefore, the symbol duration with cyclic prefix is, $N_{sym,l}^{\mu} T_c = N_{cp,l}^{\mu} T_c + N_{s,l}^{\mu} T_c$. Here $N_{s,l}^{\mu}$ denotes symbol duration without CP as $N_{s,l}^{\mu} = (l-1)\cdot 2^{-\mu+11}$. A cyclic prefix $N_{cp,l}^{\mu}$ with respect to different SCS configuration μ is commonly added to prevent inter-symbol interference. Recall SS block structure as mentioned above, the resource elements $a_{k,l}^{(p,\mu)}$ is mapped by a M-sequence $\mathbf{c}_m = [c_{m,0},...,c_{m,126}]$ at $l = 0, k \in \{56,57,...,182\}$ (PSS signal), a Gold-sequence $\mathbf{c}_{gold} = [c_{gold,0},...,c_{gold,126}]$ at $l = 0, k \in \{56,57,...,182\}$

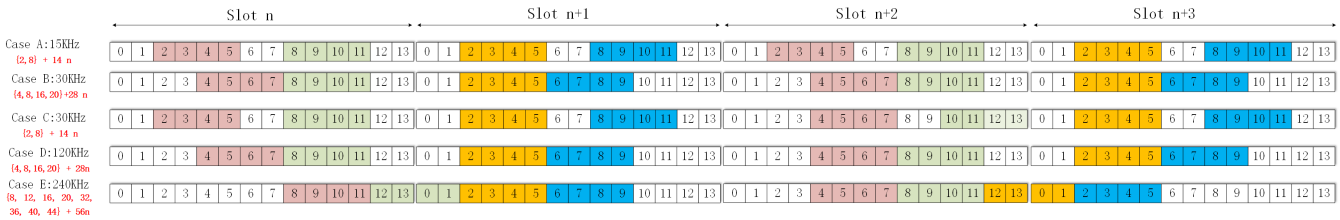

Fig. 2: Five cases of SS block pattern indicating the time location for a SS block mapping into a SS burst set are illustrated[14]. In the above cases, *ssb-PositionsInBurst* considers to be all 1. Except case B and C, the transmission pattern configurations are by SCS parameter Δf^{μ}. Pink, green, orange and blue boxes denote various SS blocks, where occupies 4 symbol each.

(SSS signal), PBCH-DMRS signal $\mathbf{c}_{pbdm}$, PBCH signal $\mathbf{c}_{pbch}$ and several 0 elements. Deployment of $\mathbf{c}_{pbdm}$ and $\mathbf{c}_{pbch}$ relate to physical CIDs.

3. AMBIGUITY FUNCTION AND SIMULATIONS

3.1. Self Ambiguity

Here we employ the wideband self ambiguity function introduced by Kelley-Wishner [15],

$$\mathcal{X}(\tau, v) = e^{j2\pi f_m \beta \tau} \left[\sqrt{\beta} \int_{-\infty}^{\infty} s(t) s^*(\beta(t-\tau)) e^{-j2\pi v t} dt \right], \tag{2}$$

where f_m denotes the carrier frequency of the SS block, β is the time stretching of the reflected signal, τ denotes the round trip delay between the BS and the target, and v denotes the Doppler spread factor. Then substituting (1) into (2), we can get

$$\begin{aligned} \mathcal{X}(\tau, v) = & \sum_{k_1=0}^{N^{\mu}-1} \sum_{k_2=0}^{N^{\mu}-1} \phi_{k_1 k_2} \sum_{l_1=0}^{L-1} \sum_{l_2=0}^{L-1} c_{k_1,l_1} c^*_{k_2,l_2} \\ & \cdot e^{j2\pi \Delta f^{\mu} (k_2 N^{\mu}_{sym,l_2} - k_1 N^{\mu}_{sym,l_1}) T_c} \end{aligned} \tag{3}$$

where

$$\phi_{k_1 k_2} = \sqrt{\beta} e^{j2\pi f_m \beta \tau} \int_{-\infty}^{\infty} e^{j2\pi t (k_1 \Delta f^{\mu} - k_2 \Delta f^{\mu} \beta - v)} dt \tag{4}$$

In case $k_1 = k_2$, the transmitted waveform is convolving with itself, therefore, (3) can be simplified to an auto-correlation function that produces the mainlobe of ambiguity function.

To evaluate the performance of a different signal structure, in this work, we simulate an NR downlink signal according to current NR standards. More exactly, the NR waveform is constructed with $\mu = 4$, where the bandwidth of each subcarrier is $\Delta f = 240$ kHz, the bandwidth of each carrier is $1656 \times \Delta f^{\mu} = 397.44$ MHz, and the symbol duration is $N^{\mu}_{sym,l} T_c = 4.46$ us. It is worth noting that this configuration can only happen in FR2 (mmWave bands). We further construct a SS block with PSS, SSS, PBCH, and PBCH-DMRS signal according to Section II. In this section, we evaluate the sensing performances of each signal structure by assuming a matched filter to themselves (PSS, SSS, PBCH, and PBCH-DMRS), the overall signal structure is the same as Fig.1. Because we are only considering the sensing performance of the specified signal structure, the rest part of the NR frame is set to zero.

According to our simulation, the zero-Doppler cut in the time domain ($\mathcal{X}(\tau, 0)$) is shown in Fig.3(a). The zero Doppler cut is dominated by the first term of $\phi_{k_1 k_2}$. In this case, the actual bandwidth of PSS, SSS, PBCH, and PBCH-DMRS are governed by their occupied subcarriers. Recall both PSS and SSS are mapped into 127 continuous subcarriers, therefore the actual bandwidth of PSS and SSS is 30.48 MHz. The corresponding sensing range resolution is $\Delta R = c/30.48 = 9.8425$ m, where c is the light speed. PBCH is mapped into all the subcarrier SS blocks. Therefore, their actual bandwidth is equal to the bandwidth of the SS block, as 57.6 MHz. Therefore, the corresponding sensing range resolution of PBCH and SS block is 5.20m. Moreover, the PBCH-DMRS is discretely allocated in SS Blocks. Therefore its actual bandwidth equals its length, which is slightly higher than PSS and SSS. The peak of the left partial view of Fig.3 (a) also confirms the superiority of SS block and PBCH on range performance. Moreover, the pulse recurrence interval (PRI) of PBCH and SS block is four symbols while PSS and SSS up to 1 (if the structure of SS block can be modified), the range ambiguity of PSS and SSS appears at $R = c/(4 \times N^{\mu}_{sym,l} T_c) = 1060$m, while the range ambiguity of PBCH and SS block is 265m.

In Fig.3(b), we examine the Doppler performance by illustrating the zero Doppler cut ($\mathcal{X}(0, v)$). This figure illustrates the Doppler performance of the deterministic NR signal structure. Theoretically, the actual Doppler resolution relies on its time duration, as $1/N^{\mu}_{sym,l} T_c \approx 22.4$kHz for PSS and SSS signal and 44.8kHz for SS block. However, lower auto-correlation property slightly suppresses the Doppler performance of the SS block. PSS, SSS, and SS block show similar Doppler performance in Fig.3 (b).

3.2. Cross Ambiguity Analysis

When a reference signal is known to receiver side, this prior can be employed as a reference signal to construct a matched

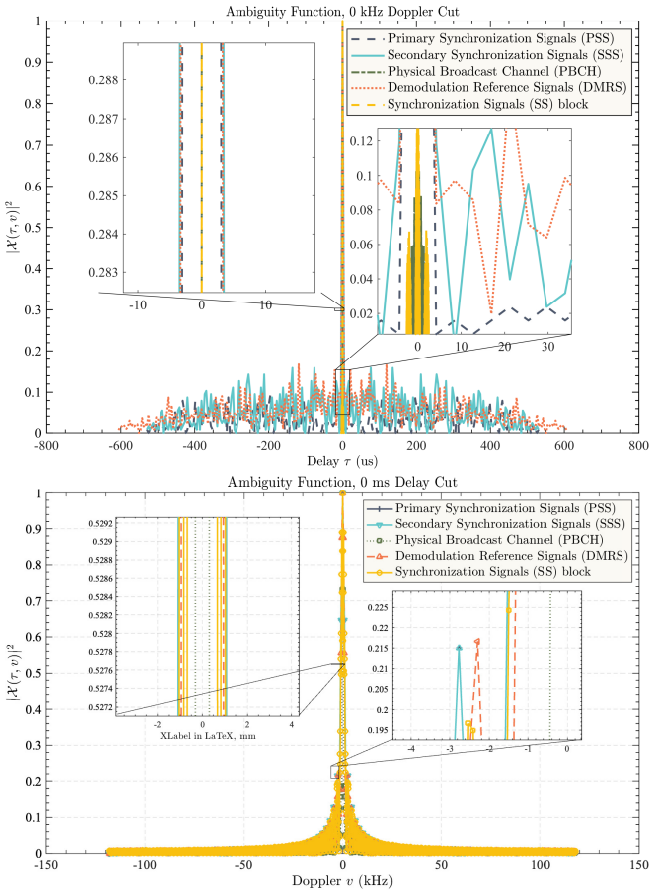

Fig. 3: (Up, a) Zero Doppler cut of the self ambiguity function of PSS, SSS, PBCH, DMRS signals and the SS block. (Down, b) Zero Delay Cut of the self ambiguity function of PSS, SSS, PBCH, DMRS signals and the SS block. The central carrier is $f_m = 24$GHz, and the numerology is μ =4.

filter, in this case, (2) can be rewritten as a cross ambiguity fiction between the received signal and the known structure,

$$\mathcal{X}(\tau, v) = e^{j2\pi f_m \beta \tau} \left[\sqrt{\beta} \int_{-\infty}^{\infty} s(t) s^*_{ref}(\beta(t-\tau)) e^{-j2\pi v t} dt \right], \tag{5}$$

where the reference signal $s_{ref}(t)$ may not be equal to received signal $s(t)$. Based on this observation, we construct a SS burst, which is defined as a group of SS blocks in release 15, and consists of 8 SS blocks under the pattern 'case E', as shown in Table 2. Intuitively, it can be regarded as a radar pulse train consists of multiple radar waveforms. Its structure is shown in the right handside of Fig.4(a).

We evaluate the cross ambiguity function in the right-hand side of Fig.4(a) by regarding PSS as a reference signal and construct a matched filter for a received SS block. The cross ambiguity shows a 'pin' shape that could achieve an acceptable range and Doppler performance. However, we also notice that the peak value is significantly lower than self ambiguity analysis. In Fig.4(b), the PSS is employed to match filtering half-frame echoes, composed of a SS burst and several random user data, reflected by a moving target plus white noise. The correlation peak periodically appears, no surprise, same with the periods of SS block, as shown on the right-hand side of Fig.4(a). However, these densely deployed peaks suppress range resolution. Again, the low peak values, 0.154, as shown in Fig.4(a), may call for a high dynamic range hardware design.

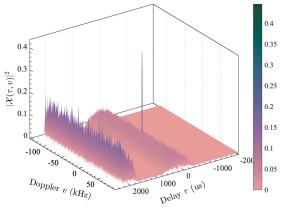

(a) Cross ambiguity between a PSS signal and a SS block.

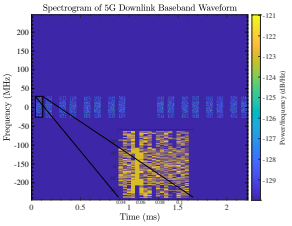

(b) The spectrogram of SS burst.

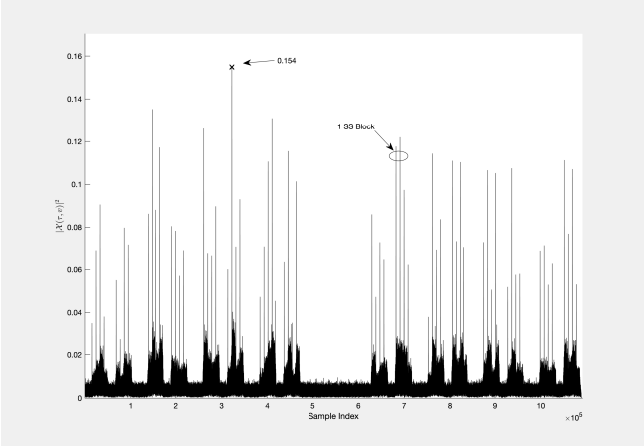

(c) Zero Doppler cut off the cross ambiguity function between a PSS signal with a SS burst, which lasts for half of an NR frame and consists of 8 SS blocks. This SS burst is conducted under the SS burst pattern case E.

Fig. 4: Cross ambiguity analysis

4. CONCLUSION

In this paper, we provided a brief overview of current NR waveform for sensing usage, and analyzed the sensing performance of NR waveforms, particularly for synchronization and reference signal. The simulation results confirm our suggestion and provide a clearer insight into the sensing performance of standardized NR waveform. Future work may include the comparison with various NR configurations. More advanced signal processing methods will also be conducted to improve the sensing resolution.

5. REFERENCES

[1] Yuanhao Cui, Fan Liu, Xiaojun Jing, and Junsheng Mu, "Integrating sensing and communications for ubiquitous iot: Applications, trends, and challenges," *IEEE Network*, vol. 35, no. 5, pp. 158–167, 2021.

[2] Fan Liu, Yuanhao Cui, Christos Masouros, Jie Xu, Tony Xiao Han, Yonina C. Eldar, and Stefano Buzzi, "Integrated sensing and communications: Towards dual-functional wireless networks for 6g and beyond," 2021.

[3] J. Andrew Zhang, Fan Liu, Christos Masouros, Robert W. Heath, Zhiyong Feng, Le Zheng, and Athina Petropulu, "An overview of signal processing techniques for joint communication and radar sensing," *IEEE Journal of Selected Topics in Signal Processing*, pp. 1–1, 2021.

[4] Weijie Yuan, Zhiqiang Wei, Shuangyang Li, Jinhong Yuan, and Derrick Wing Kwan Ng, "Integrated sensing and communication-assisted orthogonal time frequency space transmission for vehicular networks," *IEEE Journal of Selected Topics in Signal Processing*, pp. 1–1, 2021.

[5] Weijie Yuan, Fan Liu, Christos Masouros, Jinhong Yuan, Derrick Wing Kwan Ng, and Nuria González-Prelcic, "Bayesian predictive beamforming for vehicular networks: A low-overhead joint radar-communication approach," *IEEE Transactions on Wireless Communications*, vol. 20, no. 3, pp. 1442–1456, 2021.

[6] Yuanhao Cui, Visa Koivunen, and Xiaojun Jing, "Interference alignment based spectrum sharing for mimo radar and communication systems," in *2018 IEEE 19th International Workshop on Signal Processing Advances in Wireless Communications (SPAWC)*, 2018, pp. 1–5.

[7] Fan Liu, Ya-Feng Liu, Ang Li, Christos Masouros, and Yonina C. Eldar, "Cramér-rao bound optimization for joint radar-communication beamforming," *IEEE Transactions on Signal Processing*, vol. 70, pp. 240–253, 2022.

[8] Fan Liu, Christos Masouros, Athina P. Petropulu, Hugh Griffiths, and Lajos Hanzo, "Joint radar and communication design: Applications, state-of-the-art, and the road ahead," *IEEE Transactions on Communications*, vol. 68, no. 6, pp. 3834–3862, 2020.

[9] Yuanhao Cui, Visa Koivunen, and Xiaojun Jing, "Mutual information based co-design for coexisting mimo radar and communication systems," in *2020 IEEE International Conference on Communications Workshops (ICC Workshops)*, 2020, pp. 1–6.

[10] A. Evers and J. A. Jackson, "Analysis of an lte waveform for radar applications," in *2014 IEEE Radar Conference*, May 2014, pp. 0200–0205.

[11] A. Lauri, F. Colone, R. Cardinali, C. Bongioanni, and P. Lombardo, "Analysis and emulation of fm radio signals for passive radar," in *2007 IEEE Aerospace Conference*, 2007, pp. 1–10.

[12] 3GPP, "Nr; physical channels and modulation," Tech. Rep., 3GPP, April 2018.

[13] R4-1706982, "Wf on band specific ue channel bandwidth," Tech. Rep., NTT DOCOMO, 3GPP TSG RAN WG4 NR-AH-2, July 2017.

[14] Jeongho Jeon, "Nr wide bandwidth operations," *IEEE Communications Magazine*, vol. 56, no. 3, pp. 42–46, 2018.

[15] Satyabrata Sen and Arye Nehorai, "Adaptive design of ofdm radar signal with improved wideband ambiguity function," *IEEE Transactions on Signal Processing*, vol. 58, no. 2, pp. 928–933, 2009.